Effects of α-tubulin acetylation on microtubule structure and stability

Lisa Eshun-Wilson, Rui Zhang, Didier Portran, Maxence Nachury, Dan Toso, Thomas Löhr, Michele Vendruscolo, Massimiliano Bonomi, James S Fraser, Eva Nogales

Effects of α-tubulin acetylation on microtubule structure and stability

Lisa Eshun-Wilson[1], Rui Zhang[2,11], Didier Portran[3,9], Maxence Nachury[3], Dan Toso[4], Thomas Lohr[5], Michele Vendruscolo[5], Massimiliano Bonomi[5,10], James S. Fraser[6,7*] Eva Nogales[1,4,7,8*]

[1]Department of Molecular and Cellular Biology, University of California, Berkeley, CA 94720

[2]Department of Biochemistry and Molecular Biophysics, University of Washington School of Medicine, St. Louis, MO 63130

[3]Department of Ophthalmology, University of California, San Francisco, CA 94158

[4]California Institute for Quantitative Biology (QB3), University of California, Berkeley, CA 94720

[5]Department of Chemistry, University of Cambridge, CB2 1EW, UK

[6]Department of Bioengineering and Therapeutic Sciences, University of California, San Francisco, CA 94158

[7]Molecular Biophysics and Integrated Bioimaging Division, Lawrence Berkeley National Laboratory, Berkeley, CA 94720

[8]Howard Hughes Medical Institute, University of California, Berkeley, CA 94720

[9]Centre de Biologie Cellulaire de Montpellier (CRBM), CNRS, Univ. Montpellier, UMR5237, Montpellier 34090, France

[10]Current address: Structural Bioinformatics Unit, Institut Pasteur, CNRS UMR 3528, 75015 Paris, France

[11]Current address: Department of Biochemistry and Molecular Biophysics, Washington University in St. Louis, St. Louis, MO, 63110

*Co-corresponding author: jfraser@fraserlab.com

*Co-corresponding author: enogales@lbl.gov

ABSTRACT

Acetylation of K40 in α-tubulin is the sole post-translational modification to mark the luminal surface of microtubules. It is still controversial whether its relationship with microtubule stabilization is correlative or causative. We have obtained high-resolution cryo-electron microscopy reconstructions of pure samples of αTAT1-acetylated and SIRT2-deacetylated microtubules to visualize the structural consequences of this modification and reveal its potential for influencing the larger assembly properties of microtubules. We modeled the conformational ensembles of the unmodified and acetylated states by using the experimental cryo-EM density as the structural restraint in molecular dynamics simulations. We found that acetylation alters the conformational landscape of the flexible loop that contains αK40. Modification of αK40 reduces the disorder of the loop and restricts the states that it samples. We propose that the change in conformational sampling that we describe, at a location very close to the lateral contacts site, is likely to affect microtubule stability and function.

ABBREVIATIONS

MT, microtubule; PF, protofilament; PTM, post-translational modification; MAP, microtubule-associated protein; αTAT1, acetyltransferase TAT1 for α-tubulin; SIRT2 deacetylase SIRT2.

INTRODUCTION

Microtubules (MTs) are essential cytoskeletal polymers important for cell shape and motility and critical for cell division. They are built of αβ-tubulin heterodimers that assemble head-to-tail into ~13 polar protofilaments (PFs), which associate laterally to form a hollow tube[1]. Lateral contacts involve key residues in the so-called M-loop (between S7 and H9) in one tubulin monomer and the H2-H3 loop and β-hairpin structure in the H1'-S2 loop of the other tubulin subunit across the lateral interface. These lateral contacts are homotypic (α-α and β-β contacts), except at the MT "seam", where the contacts are heterotypic (α-β and β-α contacts)[2]. MTs undergo dynamic instability, the stochastic switching between growing and shrinking states[3,4]. These dynamics are highly regulated *in vivo* by multiple mechanisms that affect tubulin and its interaction with a large number of regulatory factors.

One mechanism that cells can use to manipulate MT structure and function involves the post-translational modification of tubulin subunits. Through the spatial-temporal regulation of proteins by the covalent attachment of additional chemical groups, proteolytic cleavage or intein splicing, post-translational modifications (PTMs) can play important roles in controlling the stability and function of MTs[5]. Most of tubulin PTMs alter residues within the highly flexible C-terminal tail of tubulin that extends from the surface of the MT and contributes to the binding of microtubule-associated proteins (MAPs)[6,7]. These PTMs include detyrosination, Δ2-tubulin generation, polyglutamylation, and polyglycylation[8]. However, acetylation of α-tubulin on the K40 stands out as the only tubulin PTM that localizes to the inside of the MT, within a loop of residues P37 to D47,

70 often referred to as the αK40 loop. This modification is carried out by α-tubulin
71 acetyltransferase αTAT1 and removed by the NAD^+-dependent deacetylase SIRT2 and
72 by HDAC6[6,9]. How the enzymes interact with the αK40 luminal loop, and whether this
73 "hidden PTM" has a causative or correlative effect on MT properties remain elusive.

74 Shortly after its discovery over 30 years ago[10], acetylation of αK40 was found to
75 mark stable, long-lived ($t_{1/2}$ >2 hours) MT subpopulations, including the axonemes of cilia
76 and flagella or the marginal bands of platelets[6,9], and to protect MTs from mild treatments
77 with depolymerizing drugs, such as colchicine[11] and nocodazole[12]. Multiple studies have
78 shown that reduced levels of αK40 acetylation cause axonal transport defects associated
79 with Huntington's disease, Charcot-Marie-Tooth disease, amyotrophic lateral sclerosis,
80 and Parkinson's disease[13–16]. These defects can be reversed by restoring αK40
81 acetylation levels[17]. On the other hand, elevated levels of αK40 acetylation promote cell-
82 cell aggregation, migration and tumor reattachment in multiple aggressive, metastatic
83 breast cancer cell lines[18,19].

84 Whether acetylated MTs are stable because they are acetylated or whether stable
85 structures are better at acquiring this modification remains a point of contention. For
86 example, a previous study showed that acetylation did not affect tubulin polymerization
87 kinetics *in vitro*[20]. However, this study was confounded by two factors: (i) microtubules
88 acetylated by flagellar extract were compared to native brain tubulin, which is
89 approximately 30% acetylated and (ii) only a single round of
90 polymerization/depolymerization was performed after *in vitro* acetylation, which is
91 insufficient to remove αTAT1 or other MAPs. Thus, the results of this study may be limited

by the purity and preparation of the sample. Our previous structural work also found no significant differences between 30% acetylated and 90% deacetylated MTs at a resolution of ~9 Å, particularly at the modification site, the αK40 residue within the αK40 loop, which was invisible in both cases due to the intrinsic disorder and/or to the remaining heterogeneity of the loop (i.e. that study may have been limited by the low purity of the samples)[9]. More recent *in vitro* studies, using pure samples of 96% acetylated and 99% deacetylated MTs, argue that αK40 acetylation induces a structural change that improves the flexibility and resilience of MTs[21,22]. These studies find that acetylated MTs maintain their flexural rigidity, or persistence length, after repeated rounds of mechanical stress, while deacetylated MTs show a 50% decrease in rigidity and are 26% more likely to suffer from complete breakage events[21,22].

Since the αK40 residue is less than 15 Å away from the lateral interface between protofilaments, a possible model for the molecular mechanism of acetylation is that it alters inter-protofilament interactions by promoting a conformation of the αK40 loop that confers flexural rigidity, thus increases its resistance to mechanical stress—a phenomenon called protofilament sliding[21,22]. Molecular dynamics simulations have suggested a model where αK40 forms a stabilizing salt bridge with αE55 within the core of the α-tubulin monomer that in turn stabilizes αH283 within the M-loop of its neighboring α-tubulin monomer[23]. Another study proposed that αK40 acetylation may specify 15-PF MTs, which are known to be 35% stiffer than 13PF MTs and more effective at forming microtubule bundles[24].

Given the uncertainties remaining concerning the effect of αK40 acetylation on MTs, we decided to characterize the conformational properties of the αK40 loop in the acetylated and deacetylated MTs that could have an effect on MT structure and properties. To that end, we produced near atomic-resolution cryo-EM maps of 96% acetylated (Ac^{96}) and 99% deacetylated (Ac^{0}) MTs. By improving sample purity, we were able to visualize more density for the αK40 loop in the acetylated state. Using new molecular dynamics methods, we found that acetylation shifts the conformational landscape of the αK40 loop by restricting the range of motion of the loop. In contrast, in the Ac^{0} state, the αK40 loop extends deeper into the lumen of the MT, and samples a greater number of conformations. These motions are likely to increase the accessibility of the loop to αTAT1, in agreement with the hypothesis that αTAT1 acts by accessing the MT lumen[25], and likely influence lateral contacts, in agreement with the causative effect of acetylation on the mechanical properties of microtubules[21].

RESULTS AND DISCUSSION

High-resolution cryoEM reconstructions of pure acetylated (Ac^{96}) and deacetylated (Ac^{0}) MTs

Using recent biochemical schemes designed to enrich for specific acetylation states[21], we generated Ac^{96} and Ac^{0} MTs for use in our cryo-EM studies. We prepared cryo-EM samples as previously described[2,26] of Ac^{96} and Ac^{0} MTs in the presence of end-binding protein 3 (EB3). EB3 served as a fiducial marker of the dimer that facilitated alignment of MT segments during image processing[27]. Table S1 summarizes the data

collection, refinement, and validation statistics for each high-resolution map we visualized (see also Supplemental Figures 1 and 2). Using the symmetrized MT reconstruction, which takes advantage of the pseudo-helical symmetry present in the MT, we extracted a 4x3 array of dimers for further B-factor sharpening, refinement[28], and model-building (Figure 1a). This array includes all possible lateral and longitudinal non-seam contacts for the central dimer, which was later extracted for model building and map analysis (Figure 1b,1c).

The αK40 loop has been poorly resolved in previous EM reconstructions, and existing models contain a gap between residues Pro37 and Asp48 (Supplemental Figure 3a)[25]. While the loop has been resolved in a number of X-ray crystallographic structures, the conformations stabilized in the crystal lattice are likely artifacts due to the presence of calcium and/or crystal contacts (Supplemental Figure 3b). For our symmetrized maps, we were able to build residues S38-D39 and G44-D47 into the Ac^{96} state and S38 and D46-D47 into the Ac^{0} state (Figure 1d, 1e). Qualitatively, the maps suggest that the αK40 loop is slightly more ordered in the Ac^{96} state, with the protrusion of density following Pro37 extending away from or toward Asp48 in the Ac^{96} or Ac^{0} states, respectively. However, it is likely that multiple conformations of the loop, perhaps as a function of each loop's individual position around a helical turn, are averaged together and result in the low signal-to-noise levels we observe in the map.

Conformational differences across MT states are confirmed by non-symmetrized reconstructions

We considered the possibility that the symmetrizing procedure used to improve signal and resolution in our image analysis was averaging different αK40 loop conformation within different PFs and thus interfering with our interpretation of the loop structure in the two states. To test the hypothesis, we analyzed the non-symmetrized maps calculated with C1 symmetry for the Ac^{96} and Ac^{0} states. We extracted a full turn of 13 adjacent dimers. This full-turn map revealed additional density extending out further along the loop in the Ac^{96} state when compared to the symmetrized maps filtered to the same resolution (4 Å) (Figure 2). Furthermore, the density for the loop observed at the seam was distinct from that at the non-seam contacts. To maximize the interpretability of the subunits making non-seam contacts, we used non-crystallographic symmetry (NCS) averaging as an alternative method to increase the signal-to-noise levels in the maps. This procedure improved the density for non-Glycine backbone atoms in the αK40 loop in the Ac^{96} state, allowing us to trace an initial Cα backbone for this region, while in the Ac^{0} state the loop remained unmodelable (Figure 2c, 2d). This interpretation agrees with the qualitative difference in the density, which indicate less disorder for the Ac^{96} state than Ac^{0} state, of the traditionally symmetrized and C1 maps.

This NCS averaging method had multiple advantages over the traditional averaging technique for pseudo-helical processing implemented in FREALIGN[26]. First, the model coordinates used for the averaging are based on the matrix of α-tubulin monomers along a full turn rather than the single α-tubulin monomer. Second, in the FREALIGN averaging approach the signal from the dimers at the seam are down-weighted, whereas NCS averaging allows us to separate the signal from the seam, and

thus to deconvolute the signal from the non-seam locations. Third, this procedure also acts to low-pass filter the map to 4 Å (the high-resolution limit of the C1 map, Supplemental Figure 5), which should suppress noise from the more disordered parts of the map, including alternative conformations of the αK40 loop. Using this NCS-based approach, we were able to resolve density and build a model for three additional residues, the acetylated K40, T41, and I42. These residues pack towards the globular domain of α tubulin, consistent with the favorability of burying these relatively hydrophobic residues in the Ac^{96} state. Despite observing only very weak density, we have modeled the glycine-rich region that extends into the lumen as a tight turn, which we note is only possible due to the expanded Ramachandran space accessible to glycine residues (Figure 2c). In contrast, and despite better global resolution, we did not observe any density consistent with a stable conformation of the loop in the Ac^{0} map. Based on this result, which is consistent across the NCS-averaged and traditionally symmetrized maps, we did not build any additional residues into the Ac^{0} density (Figure 2d).

Ensemble modeling of the loop in each state using density-restrained molecular dynamics

For regions that exhibit a high degree of disorder, like the αK40 loop, a single, static structure is a poor description of the native state. Ensemble models can help to elucidate how populations of conformations change upon perturbations, such as post-translational modifications[29,30]. To derive an ensemble of conformations representing the Ac^{96} and Ac^{0} states, we used the atomic structure built into the Ac^{96} map as the starting model to initiate metainference-based molecular dynamics (MD) simulations, which

augment a standard forcefield with a term representing the density derived from the EM map[31]. In contrast to Molecular Dynamics and Flexible Fitting (MDFF) and other refinement methods that seek to converge on a single structure[32], this method models a structural ensemble by maximizing the collective agreement between simulated and experimental maps, and accounts for noise using a Bayesian approach[33]. Initiating simulations for both the Ac^{96} and Ac^{0} states from starting models that differ only in the acetyl group and distinct input experimental density maps allowed us to test whether acetylation restricts the motion of the loop, trapping it in a tighter ensemble of conformations.

To analyze the conformational dynamics of the loop, we analyzed the root mean square fluctuations of residues 36-48 within replicas for each simulation. This analysis shows that the αK40 loop fluctuations are more restricted in the Ac^{96} state than in the Ac^{0} state (Figure 3a). Next, we analyzed the distribution of conformations adopted by the loop by analyzing the distance between K40 and the globular domain of α-tubulin (represented by L26) and by clustering together the snapshots from all replicas of both simulations based on the root mean square deviations of residues 36-48. Similar to the starting reference model, where the distance is 10.6 Å, Ac^{96} is enriched in conformations that pack close to the globular domain of the α-tubulin core (Figure 3b). These conformations, exemplified by clusters 1, 4, and 6, position the acetylated lysine to interact with residues along H1. In contrast, the Ac^{0} state favors conformations that extend towards the MT lumen, as exemplified by clusters 0, 2, 5, 7, and 8 (Figure 3b). Clusters 3, 9, 10, 11, labeled in grey, had equal numbers of frames enriched in Ac^{96} and Ac^{0} and sampled rare

(<5%) extreme states on both the exposed and packed ends of the conformational spectrum (Figure 3b).

These computational results are consistent with the visual analysis of the density for both the NCS and traditionally symmetrized maps, which indicated that the loop is more ordered after acetylation. The residual disorder identified by the simulations using the Ac^{96} map may be important for de-acetylation by SIRT2. On the other hand, the increased flexibility we observe for the Ac^{0} state suggests a potential mechanism by which αTAT1 could acetylate K40. Previous proposals argue that acetylation can occur from the outside or inside of the lumen[25]. However, to catalyze the modification, a flexible region within αTAT1 would have to extend approximately 25 Å through a MT wall fenestration between four tubulin dimers to reach αK40, or the MT would have to undergo a major structural rearrangement in the lattice to allow αTAT1 to enter the lumen. Previous work demonstrated that the αTAT1 active site and its MT recognition surface is concave and could not stretch through the lumen[25]. Our findings support the idea that αTAT1 modifies the loop from within the lumen of the MT because the deacetylated loop samples extended structures that would be accessible to αTAT1 and because the structural rearrangement caused by acetylation is small and local to the αK40 loop.

Acetylation induces a local structural rearrangement of the αK40 loop that promotes stability by weakening lateral contacts

Collectively our structural and MD results show that acetylation restricts the motion of the αK40 loop. These results led us to hypothesize that the change in the structural ensemble of the αK40 loop upon acetylation, while subtle and local, may affect lateral

contacts. These local changes may disrupt the small lateral interface between α-tubulin subunits. The origin of this effect may be highly distributed, as we do not visualize any stable interactions between the Ac^0 state of the loop and the globular domain. However, upon acetylation, the structural ensemble becomes more restricted and the potential for the loop to strengthen any of these interactions between monomers is lost. For example, in many of the extended conformations favored by the Ac^0 state, K40 in a α1-monomer is close to the M-loop of the neighboring α2-monomer and may buttress the H1'-S2 loop, providing support for the vital $_{\alpha1}$K60:$_{\alpha2}$H283 lateral interaction (Figure 4). In contrast, when K40 is acetylated it packs ~10 Å closer to the globular domain of the α1-monomer, reducing the potential for inter-monomer interactions (Figure 4).

We tested whether the loss of the positive charge of the lysine upon acetylation alters the electrostatic interaction energy and the hydrogen-bonding network at the lateral interface using MD simulations based on the Debye-Hückel (DH) formula[34,35]. We found that acetylation does indeed weaken lateral interactions (Supplemental Figure 4). Additionally, the Ac^0 ensemble contains conformations with strong DH interaction energies that do not exist in the Ac^{96} ensemble (Supplemental Figure 4). While the effects of acetylation are subtle, the local effects at the lateral contacts site may have an additive effect that stabilizes the MT lattice. This idea is consistent with previous work that argues that the weakening of lateral interactions is a protective mechanism to prevent pre-existing lattice defects from spreading into large areas of damage under repeated stress—a mechanism that could be exploited by cancer cells[21,22].

In conclusion, this comprehensive approach combines the structural insight of cryoEM with the sampling efficiency and global scope of MD to investigate how PTMs can transform a conformational ensemble[36,37]. Our high-resolution maps serve as a blueprint for the scale of conformational change and relevant degrees-of-freedom that the αK40 loop can sample with all-atomistic metainference MD[36]. We show that αTAT1 induces a site-specific electrostatic perturbation that restricts the motion of the loop. αK40 acetylation may function as an evolutionarily conserved 'electrostatic switch' to regulate MT stability[36,37].

MATERIALS AND METHODS

Sample Preparation for Cryo-Electron Microscopy

Porcine brain tubulin was purified as previously described[38] and reconstituted to 10 mg/ml in BRB80 buffer (80 mM 1,4-piperazinediethanesulfonic acid [PIPES], pH 6.9, 1 mM ethylene glycol tetraacetic acid [EGTA], 1 mM $MgCl_2$) with 10% (vol/vol) glycerol, 1 mM GTP, and 1 mM DTT, and flash frozen in 10 µl aliquots until needed. The acetylated and deacetylated MTs (15 µM) were co-polymerized with end-binding protein 3 (EB3, 25 µM), at 37°C for ~15 min in the presence of 10% NP-40, 1mM dithiothreitol (DTT), and BRB80 buffer. The EB3 decorated MTs were added to glow-discharged C-flat holey carbon grids (CF-1.2/1.3-4C, 400 mesh, Copper; Protochips, Morrisville, NC) inside a Vitrobot (FEI, Hillsboro, OR) set at 37°C and 85% humidity before plunge-freezing in ethane slush and liquid nitrogen, respectively, as previously described[2].

Cryo-Electron Microscopy

Micrographs were collected using a Titan Krios microscope (Thermo Fisher Scientific, Inc., Waltham, MA) operated at an accelerating voltage of 300 kV. All cryo-EM images were recorded on a K2 Summit direct electron detector (Gatan, Pleasanton, CA), at a nominal magnification of x22,500, corresponding to a calibrated pixel size of 1.07 Å. The camera was operated in super-resolution mode, with a dose rate of ~2 e^- per pixel per s on the detector. We used a total exposure time of 4 s, corresponding to a total dose of 25 electrons/$Å^2$ on the specimen. The data were collected semi-automatically using the SerialEM software suite[39].

Image Processing

Stacks of dose-fractionated image frames were aligned using the UCSF MotionCor2 software[40]. MT segments were manually selected from the drift-corrected images (acetylated dataset: 205 images, deacetylated MT dataset: 476 images) using the APPION image processing suite[41]. We estimated the CTF using CTFFIND4[42] and converted the segments to 90% overlapping boxes (512 × 512 pixels) for particle extraction. The remaining non-overlapping region is set to 80 Å and corresponds to the tubulin dimer repeat (asymmetric unit). Consequently, there are ~13 unique tubulin dimers per MT particle. To determine the initial global alignment parameters and PF number for each MT particle, raw particles were compared to 2D projections of low-passed filtered MT models (~20 Å, 4° coarse angular step size) with 12, 13, 14 and 15 PFs[43] using the multi-reference alignment (MSA) feature of EMAN1[44]. Finally, 13-PF MT particles (acetylated dataset: 20,256 particles, deacetylated MT dataset: 29,396) were refined in FREALIGN v. 9.11[45,46] using pseudo-helical symmetry to account for the

309 presence of the seam. To verify the location of the seam, we used the 40 Å shift approach
310 to categorize MTs based on their azimuthal angle, as previously described[27].

311 Atomic Model Building and Coordinate Refinement

312 COOT[47] was used to build the missing polypeptides of the αK40 loop in α-tubulin, using
313 the available PDB 3JAR as a starting model. Successively, all novel atomic models were
314 iteratively refined with phenix.real_space_refine into EM maps sharpened with
315 phenix.autosharpen[28,48]. For visual comparisons between states, potential density
316 thresholds were interactively adjusted in Coot to maximize iso-contour similarity around
317 backbone atoms distant from the αK40 loop. For Figures 1 & 2, all densities are
318 represented in Chimera at a threshold of 1.1.

319 Molecular Dynamics Simulations

320 Code for map preparation, simulation execution, and analysis is available at:
321 https://github.com/fraser-lab/plumed_em_md

322 To prepare the cryoEM maps, we fitted the maps with a Gaussian Mixture Model (GMM)
323 by applying a divide-and-conquer approach[33], using generate_gmm.py and
324 convert_GMM2PLUMED.sh. Cross-correlations to the experimental maps were greater
325 than 0.99. All simulations were performed with GROMACS 2016.5[34] and the PLUMED-
326 ISDB module[49] of the PLUMED library[50] using the Charmm36-jul2017 forcefield[51] with
327 patches for acetylated lysine (aly)[52] and the TIP3P water model. For the deacetylated
328 simulations, the same starting model was used with a manual edit of the PDB to eliminate
329 the acetylation (with all hydrogens replaced by GROMACS during model preparation).
330 The initial model was minimized then equilibrated for 2ns, using prep_plumed.py. MD
331 simulations were performed on a metainference ensemble of 8 replicas for an aggregate

simulation time of 96ns for each acetylation state, using prep_plumed2.py and prep_plumed3.py. Contributions of negative scatterers (atoms OD1 and OD2 of Asp residues; OE1 and OE2 of Glu) were excluded from contributing to the predicted maps during the simulation. This modification effectively eliminates the contribution of these side chains to the agreement between density maps, in keeping with the non-existent density of negatively charged side chains in EM maps, while allowing them to contribute to the simulation through the energy function. Clustering and convergence analyses[31] were performed and analyzed using MDAnalysis[53].

Changes in the electrostatic interaction energies at the lateral contacts were determined using the using the Debye-Hückel (DH) formula:

$$\frac{1}{4\pi\varepsilon_r\varepsilon_0}\sum_{i\epsilon A}\sum_{j\epsilon B} q_i q_j \frac{e^{-\kappa|r_{ij}|}}{|r_{ij}|}$$

where ϵ_0 is the vacuum's dielectric constant, ϵ_r the dielectric constant of the solvent, q_i and q_j the charges of the *i*-th and *j*-th atoms, respectively, $|r_{ij}|$ the distance between these two atoms, and κ is the DH parameter[35] defined in terms of the temperature T and the ionic strength of the solution I_S.

The DH energy is calculated between the following two groups of atoms, denoted as A and B in the formula above: (i) all atoms in residue range 30-60 of chain A (α1 subunit) and (ii) all atoms in residue range 200-380 of chain E (α2 subunit) in PDBs **XXYA** and **XXYB**. Residues not included in this range do not significantly contribute to the DH interaction energy between adjacent α-subunits. Parameters used in the calculation of the DH energy are: temperature (T=300K), dielectric constant of solvent (ϵ_r=80; water at room temperature), and ionic strength (I_S=1M).

ACCESSION NUMBERS

All electron density maps have been deposited in the EMDB accession numbers **EMD-X1**, **EMD-X2**, **EMD-X3**, and **EMD-X4**. Atomic models are deposited in the PDB accession numbers **XXYA**, **XXYB, XXYC**, and **XXYD, XXYE.**

AUTHOR CONTRIBUTIONS

D.P. performed the tubulin purification and modification to generate the Ac^{0} and Ac^{96} samples. L.E., R.Z., and D.T. performed the cryo-EM sample preparation, electron microscopy and data processing. L.E. and J.S.F. engineered the NCS-averaging technique, performed iterative model-building/refinement. L.E., J.S.F., T. L., M. V. and M.B. executed the metainference MD simulations. All authors contributed to structure interpretation, model development and manuscript writing.

ACKNOWLEDGEMENTS

We thank P. Grob and J. Fang for cryo-EM data collection support, A. Chintangal and P. Tobias for computational support, and E. Kellogg, B. LaFrance, S. Howes, T.H.D. Nguyen, S. Pöpsel, B. Greber, and K. Morris for helpful discussions. We also acknowledge the Berkeley Bay Area Cryo-EM (BACEM) Facility and additional scientific resources at UC Berkeley. J.S.F was funded by the UCSF-UCB Sackler Faculty Exchange Program and NIGMS grant R01- GM123159. This work was funded through NIGMS grants R01-GM63072 to E.N. and the NSF grant 2016222703 and the NAS NRC Ford Foundation grant to L.E. E.N. is a Howard Hughes medical investigator.

REFERENCES

1. Nogales, E., Whittaker, M., Milligan, R. A. & Downing, K. H. High-resolution model of the microtubule. *Cell* (1999). doi:10.1016/S0092-8674(00)80961-7
2. Zhang, R., Alushin, G. M., Brown, A. & Nogales, E. Mechanistic origin of microtubule dynamic instability and its modulation by EB proteins. *Cell* (2015). doi:10.1016/j.cell.2015.07.012
3. Mitchison, T. J. Localization of an exchangeable GTP binding site at the plus end of microtubules. *Science (80-.).* (1993). doi:10.1126/science.8102497
4. Mitchison, T. & Kirschner, M. Dynamic instability of microtubule growth. *Nature* (1984). doi:10.1038/312237a0
5. Walsh, G. & Jefferis, R. Post-translational modifications in the context of therapeutic proteins. *Nature Biotechnology* (2006). doi:10.1038/nbt1252
6. Magiera, M. M., Singh, P., Gadadhar, S. & Janke, C. Tubulin Posttranslational Modifications and Emerging Links to Human Disease. *Cell* (2018). doi:10.1016/j.cell.2018.05.018
7. Janke, C. & Montagnac, G. Causes and Consequences of Microtubule Acetylation. *Curr. Biol.* **27,** R1287–R1292 (2017).
8. Janke, C. & Bulinski, J. C. Post-translational regulation of the microtubule cytoskeleton: Mechanisms and functions. *Nature Reviews Molecular Cell Biology* (2011). doi:10.1038/nrm3227
9. Howes, S. C., Alushin, G. M., Shida, T., Nachury, M. V. & Nogales, E. Effects of tubulin acetylation and tubulin acetyltransferase binding on microtubule structure. *Mol. Biol. Cell* (2014). doi:10.1091/mbc.E13-07-0387
10. LeDizet, M. & Piperno, G. Identification of an acetylation site of Chlamydomonas alpha-tubulin. *Proc. Natl. Acad. Sci.* (1987). doi:10.1073/pnas.84.16.5720
11. LeDizet, M. & Piperno, G. Cytoplasmic microtubules containing acetylated α-tubulin in Chlamydomonas reinhardtii: Spatial arrangement and properties. *J. Cell Biol.* (1986). doi:10.1083/jcb.103.1.13
12. De Brabander, M. J., Van de Veire, R. M. L., Aerts, F. E. M., Borgers, M. & Janssan, P. A. J. The Effects of Methyl [5-(2-Thienylcarbonyl)-1H-benzimidazol-2-yl]carbamate, (R 17934; NSC 238159), a New Synthetic Antitumoral Drug Interfering with Microtubules, on Mammalian Cells Cultured in Vitro. *Cancer Res.* (1976).
13. Dompierre, J. P. *et al.* Histone Deacetylase 6 Inhibition Compensates for the Transport Deficit in Huntington's Disease by Increasing Tubulin Acetylation. *J. Neurosci.* (2007). doi:10.1523/JNEUROSCI.0037-07.2007
14. D'Ydewalle, C. *et al.* HDAC6 inhibitors reverse axonal loss in a mouse model of mutant HSPB1-induced Charcot-Marie-Tooth disease. *Nat. Med.* (2011). doi:10.1038/nm.2396
15. Kim, J. Y. *et al.* HDAC6 Inhibitors Rescued the Defective Axonal Mitochondrial Movement in Motor Neurons Derived from the Induced Pluripotent Stem Cells of Peripheral Neuropathy Patients with HSPB1 Mutation. *Stem Cells Int.* (2016). doi:10.1155/2016/9475981

16. Li, L. *et al.* MEC-17 Deficiency Leads to Reduced -Tubulin Acetylation and Impaired Migration of Cortical Neurons. *J. Neurosci.* (2012). doi:10.1523/JNEUROSCI.0016-12.2012
17. Godena, V. K. *et al.* Increasing microtubule acetylation rescues axonal transport and locomotor deficits caused by LRRK2 Roc-COR domain mutations. *Nat. Commun.* (2014). doi:10.1038/ncomms6245
18. Boggs, A. E. *et al.* α-Tubulin acetylation elevated in metastatic and basal-like breast cancer cells promotes microtentacle formation, adhesion, and invasive migration. *Cancer Res.* (2015). doi:10.1158/0008-5472.CAN-13-3563
19. Di Martile, M., Del Bufalo, D. & Trisciuoglio, D. The multifaceted role of lysine acetylation in cancer: prognostic biomarker and therapeutic target. *Oncotarget* (2015). doi:10.18632/oncotarget.10048
20. Maruta, H., Greer, K. & Rosenbaum, J. L. The acetylation of alpha-tubulin and its relationship to the assembly and disassembly of microtubules. *J. Cell Biol.* (1986). doi:10.1083/jcb.103.2.571
21. Portran, D., Schaedel, L., Xu, Z., Théry, M. & Nachury, M. V. Tubulin acetylation protects long-lived microtubules against mechanical ageing. **19,** (2017).
22. Xu, Z. *et al.* Microtubules acquire resistance from mechanical breakage through intralumenal acetylation. *Science (80-.).* (2017). doi:10.1126/science.aai8764
23. Cueva, J. G., Hsin, J., Huang, K. C. & Goodman, M. B. Posttranslational acetylation of α-tubulin constrains protofilament number in native microtubules. *Curr. Biol.* (2012). doi:10.1016/j.cub.2012.05.012
24. Chaaban, S. & Brouhard, G. J. A microtubule bestiary: structural diversity in tubulin polymers. *Mol. Biol. Cell* **28,** 2924–2931 (2017).
25. Szyk, A. *et al.* Molecular basis for age-dependent microtubule acetylation by tubulin acetyltransferase. *Cell* (2014). doi:10.1016/j.cell.2014.03.061
26. Alushin, G. M. *et al.* High-Resolution microtubule structures reveal the structural transitions in αβ-tubulin upon GTP hydrolysis. *Cell* (2014). doi:10.1016/j.cell.2014.03.053
27. Zhang, R. & Nogales, E. A new protocol to accurately determine microtubule lattice seam location. *J. Struct. Biol.* (2015). doi:10.1016/j.jsb.2015.09.015
28. Adams, P. D. *et al.* PHENIX: A comprehensive Python-based system for macromolecular structure solution. *Acta Crystallogr. Sect. D Biol. Crystallogr.* (2010). doi:10.1107/S0907444909052925
29. Bonomi, M. & Vendruscolo, M. Determination of protein structural ensembles using cryo-electron microscopy. 1–22 (2018).
30. Vahidi, S. *et al.* Reversible inhibition of the ClpP protease via an N-terminal conformational switch. *Proc. Natl. Acad. Sci.* (2018). doi:10.1073/pnas.1805125115
31. Bonomi, M., Pellarin, R. & Vendruscolo, M. Simultaneous Determination of Protein Structure and Dynamics Using Cryo-Electron Microscopy. *Biophys. J.* (2018). doi:10.1016/j.bpj.2018.02.028
32. Singharoy, A. *et al.* Molecular dynamics-based refinement and validation for sub-5 Å cryo-electron microscopy maps. *Elife* (2016). doi:10.7554/eLife.16105
33. Hanot, S. *et al.* Multi-scale Bayesian modeling of cryo-electron microscopy density maps. *bioRxiv* (2017). doi:10.1101/113951

34. Hess, B., Kutzner, C., Van Der Spoel, D. & Lindahl, E. GRGMACS 4: Algorithms for highly efficient, load-balanced, and scalable molecular simulation. *J. Chem. Theory Comput.* (2008). doi:10.1021/ct700301q
35. Do, T. N., Carloni, P., Varani, G. & Bussi, G. RNA/peptide binding driven by electrostatics - Insight from bidirectional pulling simulations. *J. Chem. Theory Comput.* (2013). doi:10.1021/ct3009914
36. Narayanan, A. & Jacobson, M. P. Computational studies of protein regulation by post-translational phosphorylation. *Current Opinion in Structural Biology* (2009). doi:10.1016/j.sbi.2009.02.007
37. Beltrao, P. *et al.* Evolution and functional cross-talk of protein post-translational modifications. *Mol. Syst. Biol.* (2013). doi:10.1002/msb.201304521
38. Castoldi, M. & Popov, A. V. Purification of brain tubulin through two cycles of polymerization- depolymerization in a high-molarity buffer. *Protein Expr. Purif.* (2003). doi:10.1016/S1046-5928(03)00218-3
39. Mastronarde, D. N. Automated electron microscope tomography using robust prediction of specimen movements. *J. Struct. Biol.* (2005). doi:10.1016/j.jsb.2005.07.007
40. Zheng, S., Palovcak, E., Armache, J.-P., Cheng, Y. & Agard, D. Anisotropic Correction of Beam-induced Motion for Improved Single-particle Electron Cryo-microscopy. *bioRxiv* (2016). doi:10.1101/061960
41. Lander, G. C. *et al.* Appion: An integrated, database-driven pipeline to facilitate EM image processing. *J. Struct. Biol.* (2009). doi:10.1016/j.jsb.2009.01.002
42. Rohou, A. & Grigorieff, N. CTFFIND4: Fast and accurate defocus estimation from electron micrographs. *J. Struct. Biol.* (2015). doi:10.1016/j.jsb.2015.08.008
43. Egelman, E. H. The iterative helical real space reconstruction method: Surmounting the problems posed by real polymers. *J. Struct. Biol.* (2007). doi:10.1016/j.jsb.2006.05.015
44. Ludtke, S. J., Baldwin, P. R. & Chiu, W. EMAN: Semiautomated software for high-resolution single-particle reconstructions. *J. Struct. Biol.* (1999). doi:10.1006/jsbi.1999.4174
45. Lyumkis, D., Brilot, A. F., Theobald, D. L. & Grigorieff, N. Likelihood-based classification of cryo-EM images using FREALIGN. *J. Struct. Biol.* (2013). doi:10.1016/j.jsb.2013.07.005
46. Grigorieff, N. FREALIGN: High-resolution refinement of single particle structures. *J. Struct. Biol.* (2007). doi:10.1016/j.jsb.2006.05.004
47. Emsley, P., Lohkamp, B., Scott, W. G. & Cowtan, K. Features and development of Coot. *Acta Crystallogr. Sect. D Biol. Crystallogr.* (2010). doi:10.1107/S0907444910007493
48. Terwilliger, T. C. *et al.* Automated map sharpening by maximization of detail and connectivity Bioscience Division , Los Alamos National Laboratory , Mail Stop M888 , Los Alamos , NM , Molecular Biophysics and Integrated Bioimaging Division , Lawrence Berkeley National. (2018).
49. Bonomi, M. & Camilloni, C. Integrative structural and dynamical biology with PLUMED-ISDB. *Bioinformatics* (2017). doi:10.1093/bioinformatics/btx529
50. Tribello, G. A., Bonomi, M., Branduardi, D., Camilloni, C. & Bussi, G. PLUMED 2: New feathers for an old bird. *Comput. Phys. Commun.* (2014).

doi:10.1016/j.cpc.2013.09.018

51. Huang, J. & Mackerell, A. D. CHARMM36 all-atom additive protein force field: Validation based on comparison to NMR data. *J. Comput. Chem.* (2013). doi:10.1002/jcc.23354

52. Huang, J. *et al.* CHARMM36m: An improved force field for folded and intrinsically disordered proteins. *Nat. Methods* (2016). doi:10.1038/nmeth.4067

53. Michaud-Agrawal, N., Denning, E. J., Woolf, T. B. & Beckstein, O. MDAnalysis: A toolkit for the analysis of molecular dynamics simulations. *J. Comput. Chem.* (2011). doi:10.1002/jcc.21787

FIGURE LEGENDS

Figure 1. High-resolution maps of 96% acetylated (Ac^{96}) and <1% acetylated (Ac^{0}) microtubules. (a) Schematic of the model-building and refinement process in PHENIX. We sharpened a representative 4x3 lattice, refined the corresponding atomic structure (3JAR) into our map, and extracted out the central dimer to build additional residues into the αK40 loop. We performed this process iteratively for both the Ac^{96} and Ac^{0}. The structure of the Ac^{96} **(b)** and Ac^{0} **(c)** αβ-tubulin heterodimers, respectively, are shown from the outer and luminal views with close-ups of αK40 loop in each state **(d)** and **(e)** low-pass filtered to 3.7 Å.

Figure 2. Symmetrized and NCS-averaged C1 maps of Ac^{96} and Ac^{0} microtubules reveal the αK40 loop is more ordered in the Ac^{96} state. Close-up views of the αK40 loop (P37-D47) in the **(a)** Ac^{96} and **(b)** Ac^{0} states in the symmetrized maps low-pass filtered to 4 Å and the **(c)** Ac^{96} and **(d)** Ac^{0} states in the NCS averaged C1 maps low-pass filtered to 4 Å. Dotted lines indicate missing residues.

Figure 3. Acetylation restricts the motion and alters the conformational ensemble of the αK40 loop. (a) Per-residue root mean square fluctuations (RMSF) analyses were determined over the course of 12 ns for residues 34-50 the C1 maps using GROMACs in PLUMED and graphed using the MDAnalysis. (b) Ensemble modeling of the loop across Ac^{96} and Ac^{0} states using density restrained MD. Frames were classified into one of 11 clusters by conformation. Clusters either had a greater number of Ac^{96} frames (red), Ac^{0} frames (blue), or an equal number of frames from both states (grey). The reference is

551 shown in green. The unique conformations of each of the 11 clusters are shown to the
552 right.
553
554 **Figure 4. Acetylation may weaken lateral interactions.** Close-up view of the lateral
555 contacts between two α-tubulin monomers at a non-seam location (α1, light green; α2,
556 dark green). K40 in α1 of the Ac^0 state is 8 Å closer to the M-loop of α2 and appears to
557 buttress the H1'-S2 loop, providing support for the vital α1K60-α2H283 lateral interaction.
558 By contrast, that support is lost in the Ac^{96} state because the acetylated K40 now packs
559 much closer to the hydrophobic, inner core.
560
561 **Supplemental Figure 1. Schematic of the experimental workflow for sample**
562 **preparation and pseudo-helical image processing.** EB3 decorated MTs were added
563 to glow-discharged C-flat holey carbon grids (CF-1.2/1.3-4C, 400 mesh, Copper;
564 Protochips, Morrisville, NC) inside a Vitrobot (FEI, Hillsboro, OR) set at 37°C and 85%
565 humidity before plunge-freezing in ethane slush and liquid nitrogen. Images were
566 collected with the Titan Krios electron microscope (Thermo Fisher Scientific, Inc.,
567 Waltham, MA) operated at 300kV and equipped with a K2 direct detector (Gatan,
568 Pleasanton, CA). The micrographs were collected at a nominal magnification of
569 x22,500. Stacks of dose-fractionated image frames were aligned using the UCSF
570 MotionCor2 software and CTF-corrected with CTFFIND4. MT segments were manually
571 selected and converted to 90% overlapping boxes (512 × 512 pixels) for particle
572 extraction. The remaining non-overlapping region is set to 80 Å and corresponds to the
573 tubulin dimer repeat (asymmetric unit). These raw particles were compared to 2D

574 projections of low-passed filtered MT models (~20 Å, 4° coarse angular step size) with
575 13 and 14 PFs using the multi-reference alignment (MRA) feature of EMAN1. Next, 13-
576 PF MT particles were refined in FREALIGN v. 9.11 using pseudo-helical symmetry to
577 account for the presence of the seam. To verify the location of the seam, MTs were
578 categorized based on their azimuthal angle and refined again.
579
580 **Supplemental Figure 2. Sample preparation, data collection and image**
581 **processing of acetylated and deacetylated MT samples. (a)** Ac^{96} and Ac^{0} tubulin
582 preparations were produced by treating purified mammalian brain tubulin (Ac^{30}) with
583 acetyltransferase αTAT1 and deacetylatase SIRT2. Samples were resolved on SDS-
584 page and Coomassie-stained (top panel) or immunoblotted for αK40 acetylation (bottom
585 panel). Axomenal preparations from Tetrahymena cilia provide a 100% acetylation
586 calibrator. Adapted from Portran[21]. **(b)** Representative cryo-EM images of acetylated, in
587 the left panel, and deacetylated MTs, in the right panel. Scale bar = 200 nm. Images
588 were collected with the Titan Krios electron microscope (FEI, Hillsboro, OR) operated at
589 300kV and equipped with a K2 direct detector (Gatan, Pleasanton, CA). The
590 micrographs were collected at a nominal magnification of 22,500x, resulting in a final
591 pixel size of 1.07 Å per pixel and dose rate of 8 e-/pixel/s. **(c)** Schematic of data
592 collection. Using EB3, we generated >80% homogeneous samples to push the
593 resolution to ~3.5 Å.
594
595 **Supplemental Figure 3. Previous proposed αK40 loop models. (a)** Published PDBs
596 with incomplete models of the loop: 5NQU (Chain A), 5EYP (Chain A), 3RYC (Chain A),

3RYC (Chain C), 5NQT (Chain A), 3RYI (Chain A), 3RYI (Chain A), 3RYF (Chain A), 3RYF (Chain C). **(b)** Example of the a published PDB with the complete loop stabilized by calcium: 5YL4 (Chain C).

Supplemental Figure 4. Acetylation weakens lateral interactions. By analyzing the distribution of Debye-Hückel (DH) electrostatic energy between adjacent α-subunits across the AC0 (blue) and AC96 ensembles (red), we find that acetylation weakens lateral interactions. The DH energy is calculated between the following two groups of atoms: (i) all atoms in residue range 30-60 of chain A (α1 subunit) and (ii) all atoms in residue range 200-380 of chain E (α2 subunit) in PDBs **XXYA** and **XXYB.** The plot shows the probability density function, or Pdf, as a function of the DH interaction energy.

Supplemental Figure 5. Fourier Shell Correlation Plots.
The $FSC_{half\text{-}map}$ resolution, using **0.143** as the gold standard criterion, represents how well the two half-maps from each dataset correlate as a function of spatial frequency. The two half-maps were generated by dividing the final dataset into two independent 3D-reconstructions. The $FSC_{map\ vs.\ model}$ resolution, using **0.5** as the gold standard criterion, represents how well the final map correlated with the refined atomic model. All plots were generated in PHENIX.

SUPPLEMENTAL TABLE 1. CryoEM data collection, refinement parameters, and validation statistics.

Parameters	**Ac^{96} Symmetrized (EMDB-#, PDB-#)**	**Ac^{0} Symmetrized (EMDB-#, PDB-#)**	**Ac^{96} C1 (EMDB-#, PDB-#)**	**Ac^{0} C1 (EMDB-#, PDB-#)**
Magnification	22500x	22500x	22500x	22500x
Voltage	300	300	300	300
Electron exposure (e-/A^2)	25	25	25	25
Defocus range (μm)	-1.5 to -2.5	-1.5 to -2.5	-1.5 to -2.5	-1.5 to -2.5
Pixel size (Å)	1.07 Å	1.07 Å	1.07 Å	1.07 Å
Symmetry imposed	HP	HP	C1	C1
Initial particle images (no.)	20256	29396	20256	29396
Final particle images (no.)	18432	24692	18432	24692
Helical Rise			9.3	9.3
Helical Twist			27.7	27.7
Dimer Rise (Å)			80.5	81
Dimer Twist			-0.12º	-0.12º
Map resolution (Å)	**3.3**	**3.7**	**4.1**	**4.0**
FSC threshold	0.143	0.143	0.143	0.143
Map resolution range (Å)	3.5-4.1 Å	3.0-3.6 Å	3.8-5.4 Å	3.5-4.5 Å
Refinement				
Initial model used (PDB ID)	3JAR	3JAR	3JAR	3JAR

Model resolution (Å)	4 Å	3.6 Å	6 Å	5.8 Å
FSC threshold	0.5	0.5	0.5	0.5
Map sharpening method	*Phenix_auto_sharpen*	*Phenix_auto_sharpen*	*Phenix_auto_sharpen*	*Phenix_auto_sharpen*
Model composition				
Nonhydrogen atoms	40866	40866	320775	320775
Protein residues	5184	5184	40702	40702
Ligands (GTP, GDP)	12	12	94	94
B factors (Å^2)				
Protein	126.11	96.80	193.47	161.40
Ligand	122.25	89.44	192.42	156.32
Bond lengths: RMS (deviation)	0.007	0.007	0.007	0.006
Bond angles: RMS (deviation)	1.110	1.107	1.110	1.112
Validation				
MolProbity score	1.57	1.63	1.80	1.78
Clashscore	6.64	6.64	9.15	8.92
Rotamer outliers (%)	0.14	0.41	0.14	0.14
Ramachandran plot				
Favored (%)	96.74	96.18	95.48	95.6
Outliers (%)	0	0	0	0

621

622

GRAPHICAL ABSTRACT

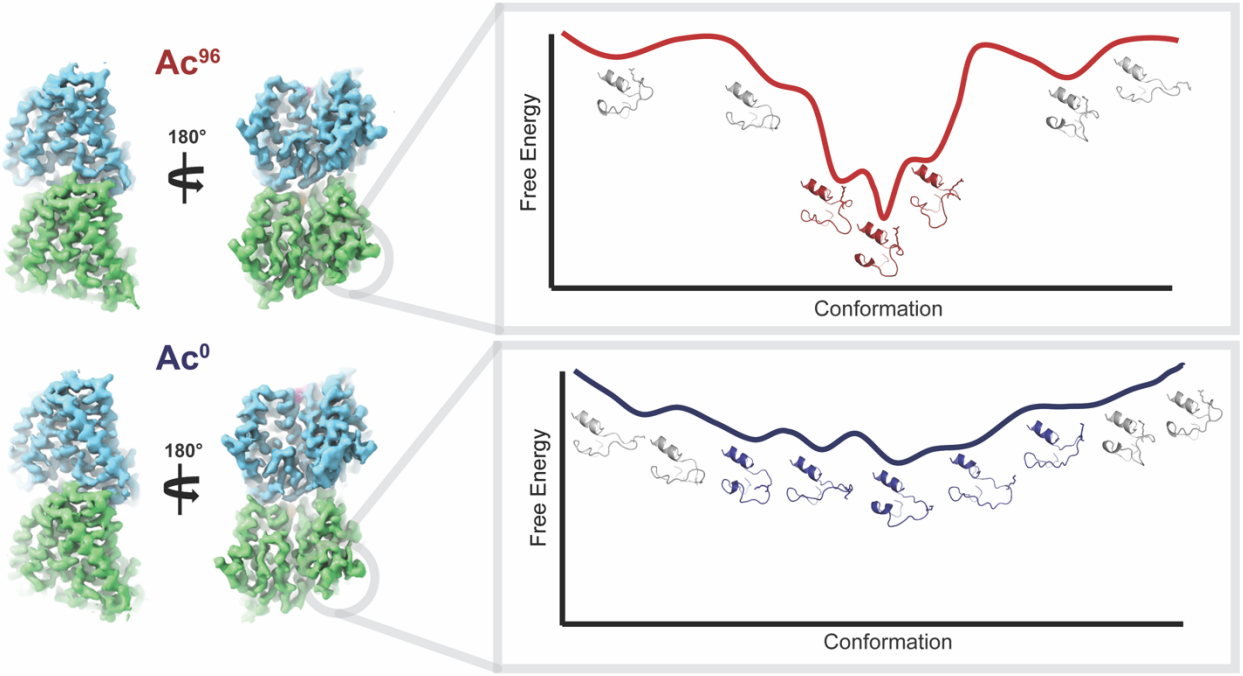

623 Acetylation alters the structural ensemble of the αK40 loop of α-tubulin.

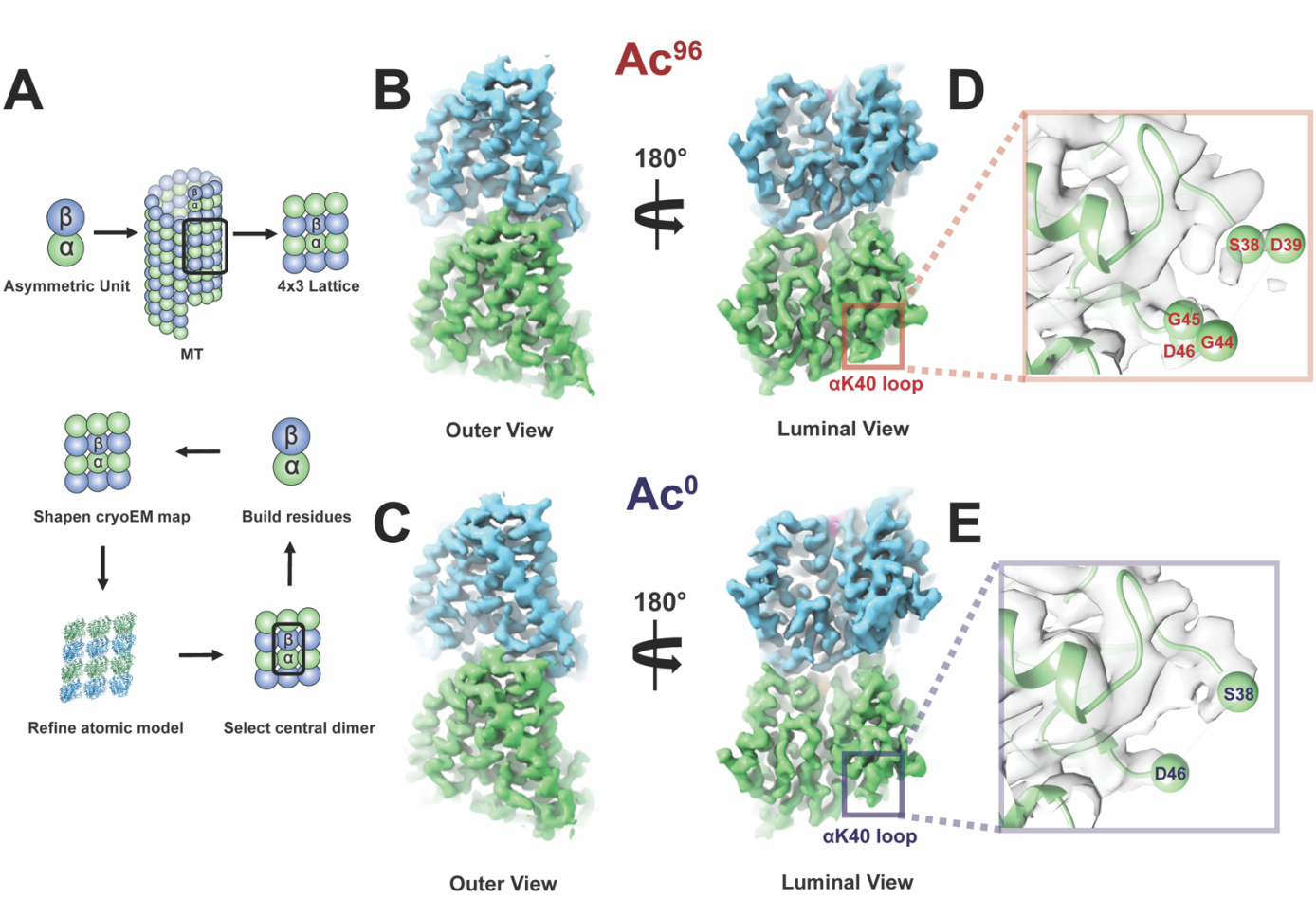

Figure 1. High-resolution maps of 96% acetylated (Ac^{96}) and <1% acetylated (Ac^{0}) microtubules.

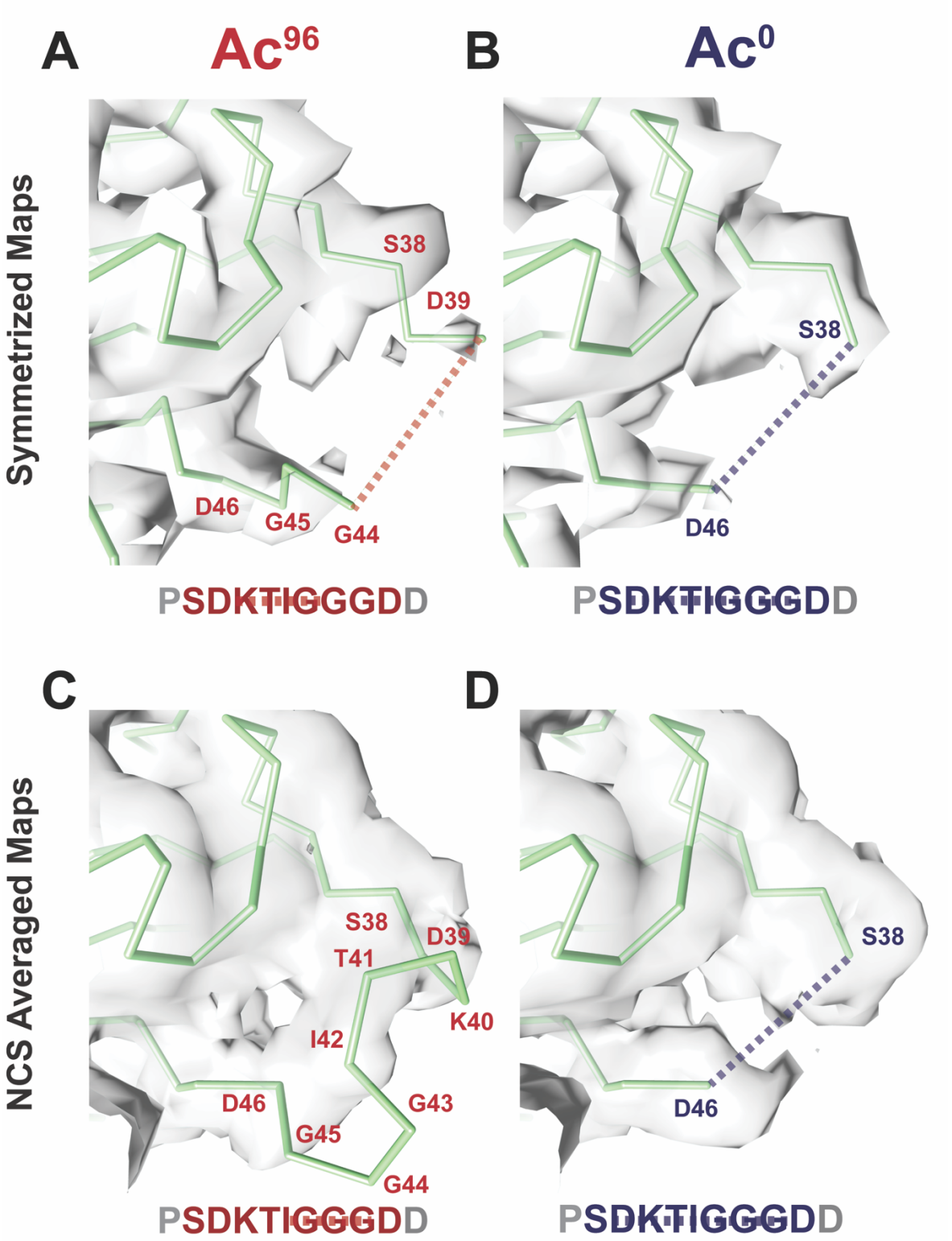

627

628 **Figure 2. Symmetrized and NCS-averaged C1 maps of Ac^{96} and Ac^{0} microtubules**

629 **reveal the αK40 loop is more ordered in the Ac^{96} state.**

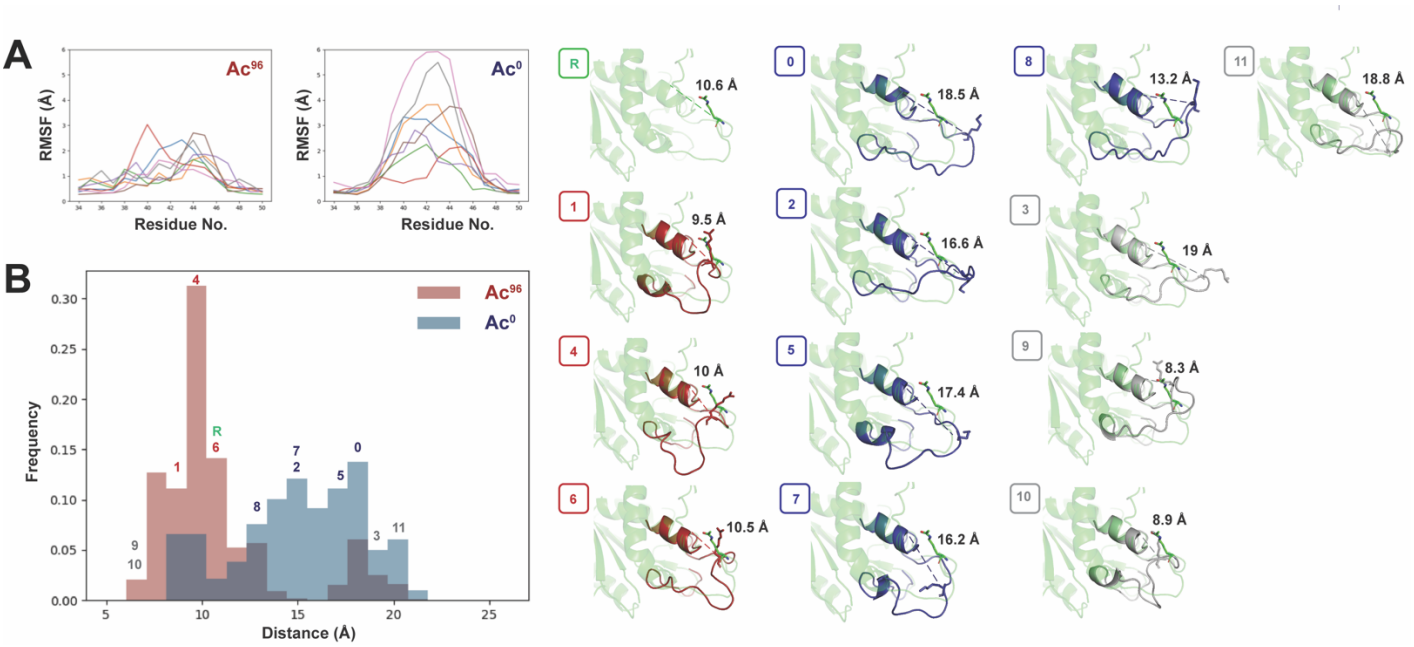

Figure 3. Acetylation restricts the motion and alters the conformational ensemble of the αK40 loop.

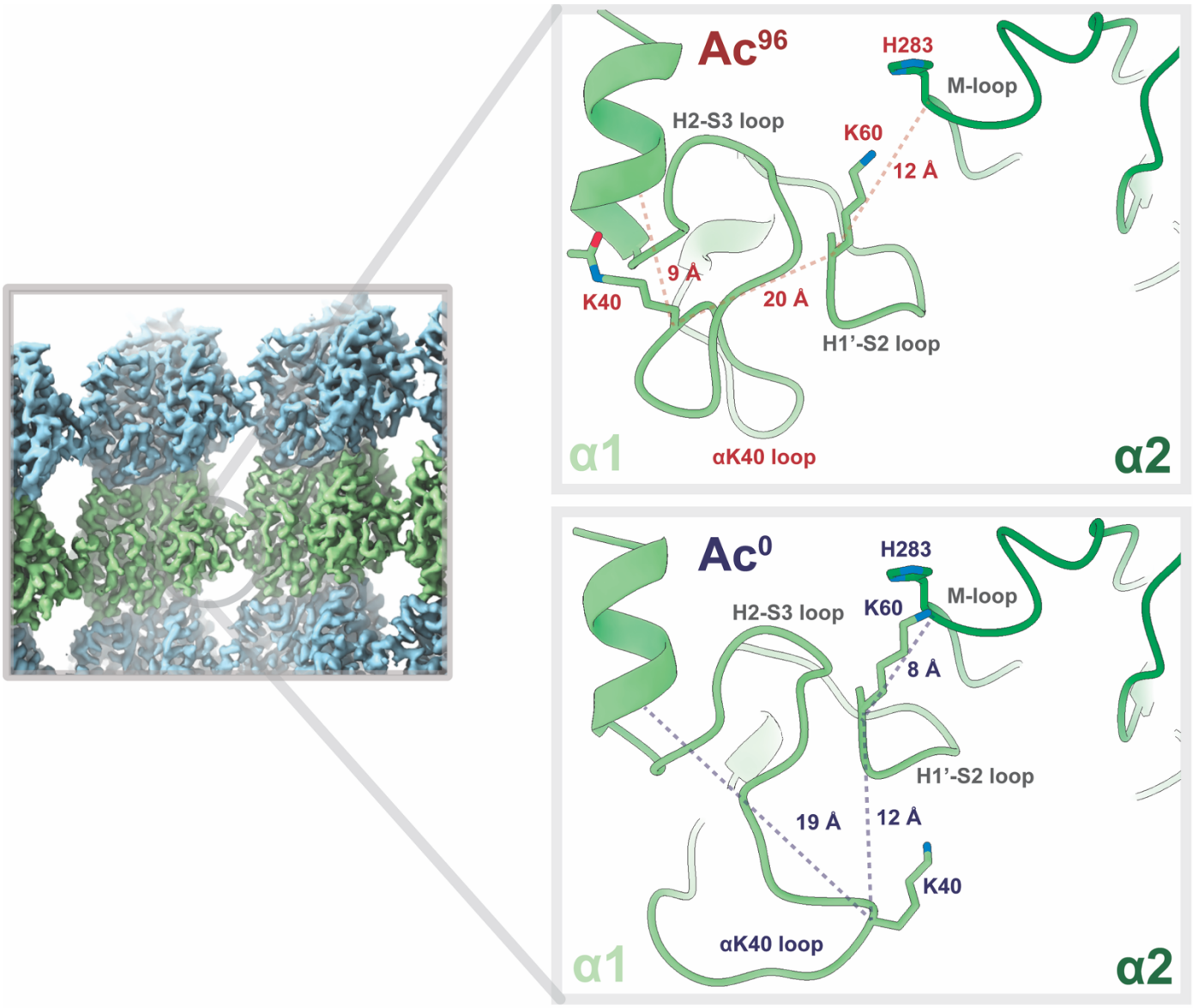

633

634 **Figure 4. Acetylation may weaken lateral interactions.**

635

636

637

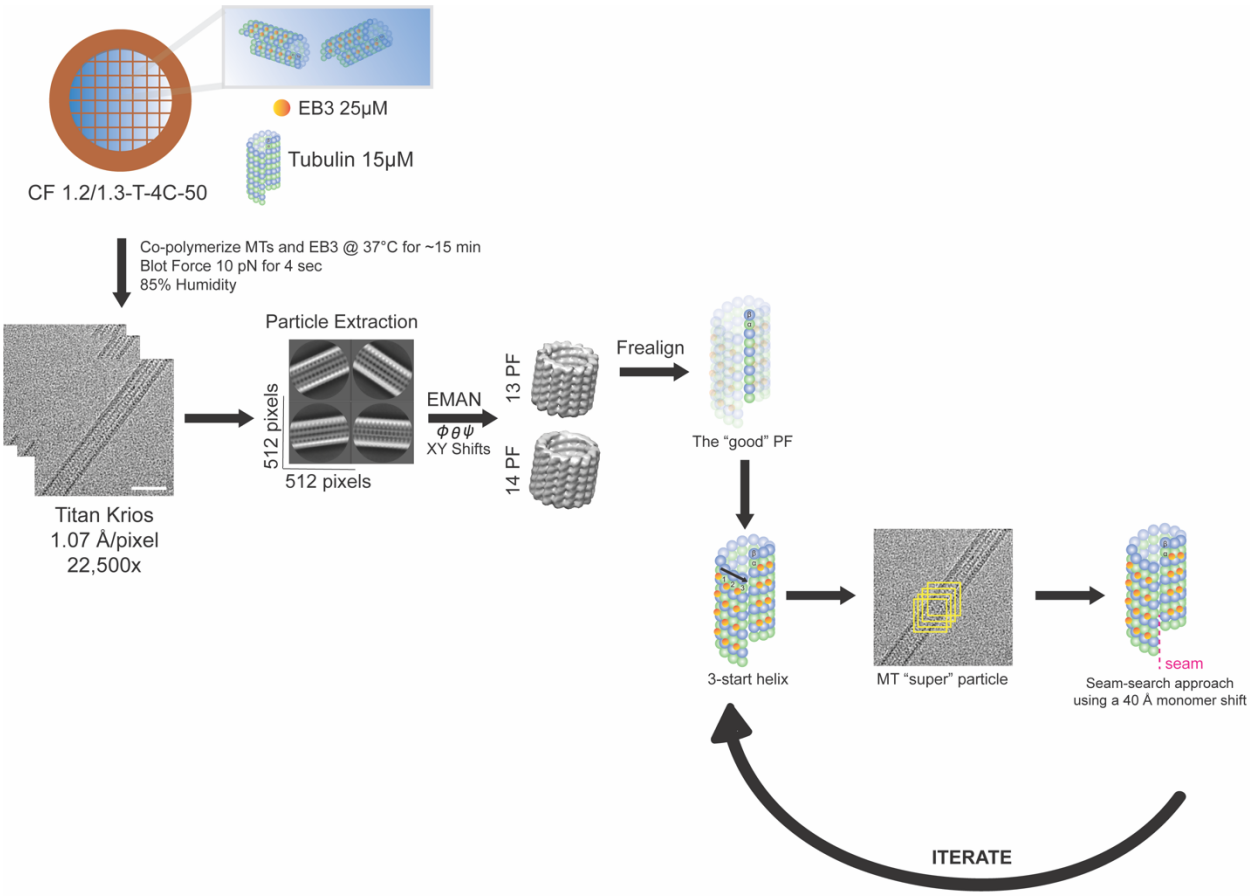

638

639 **Supplemental Figure 1. Schematic of the experimental workflow for sample**

640 **preparation and pseudo-helical image processing.**

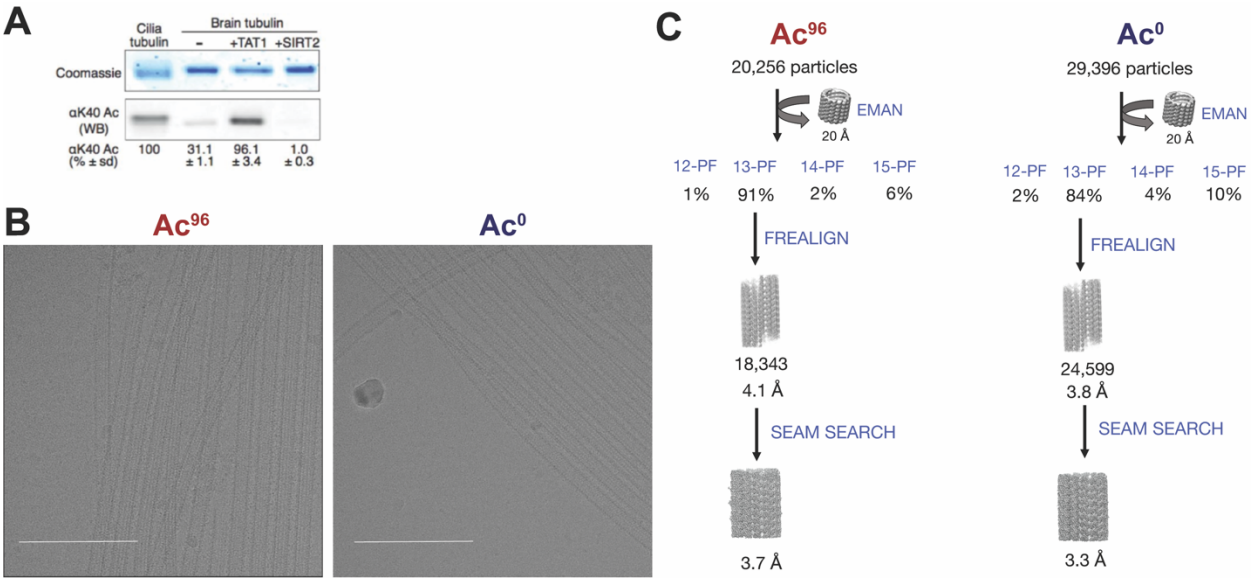

641

642 **Supplemental Figure 2. Sample preparation, data collection and image**

643 **processing of acetylated and deacetylated MT samples.**

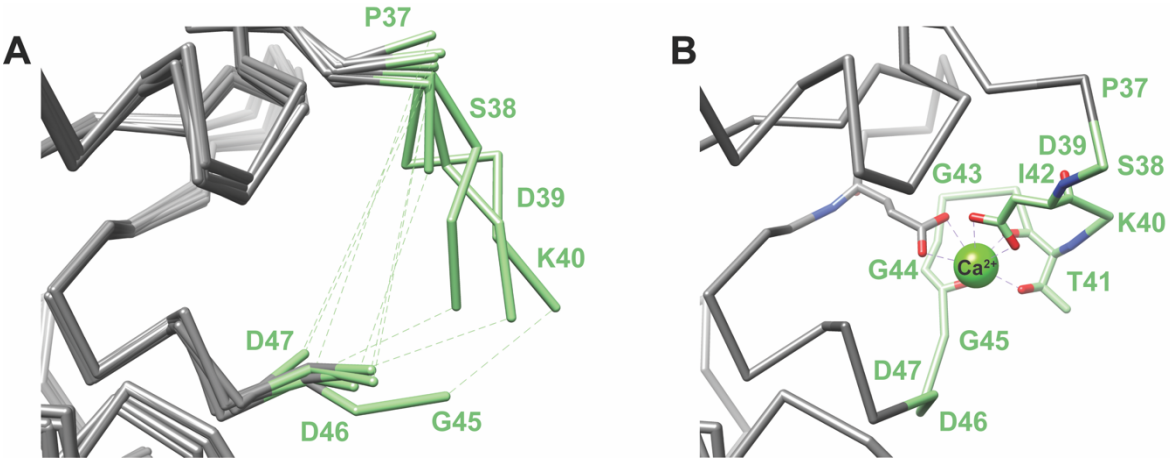

644

645 **Supplemental Figure 3. Previous proposed αK40 loop models.**

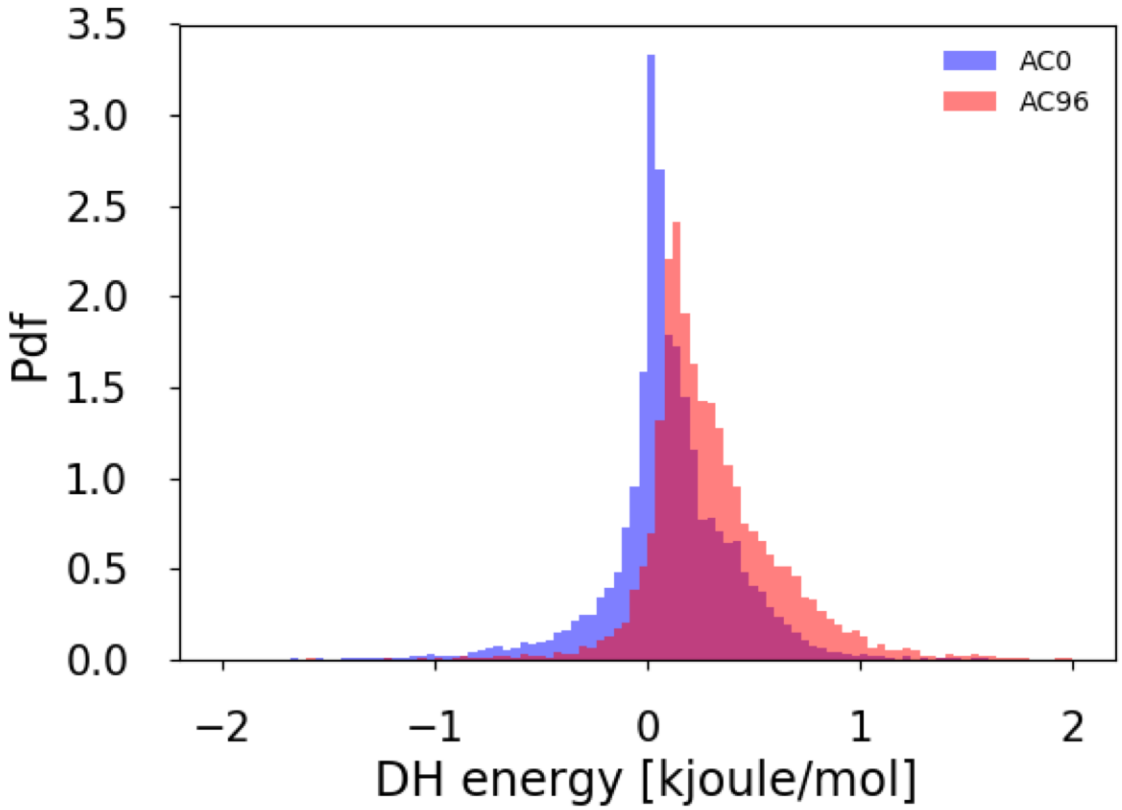

Supplemental Figure 4. Acetylation weakens lateral interactions.

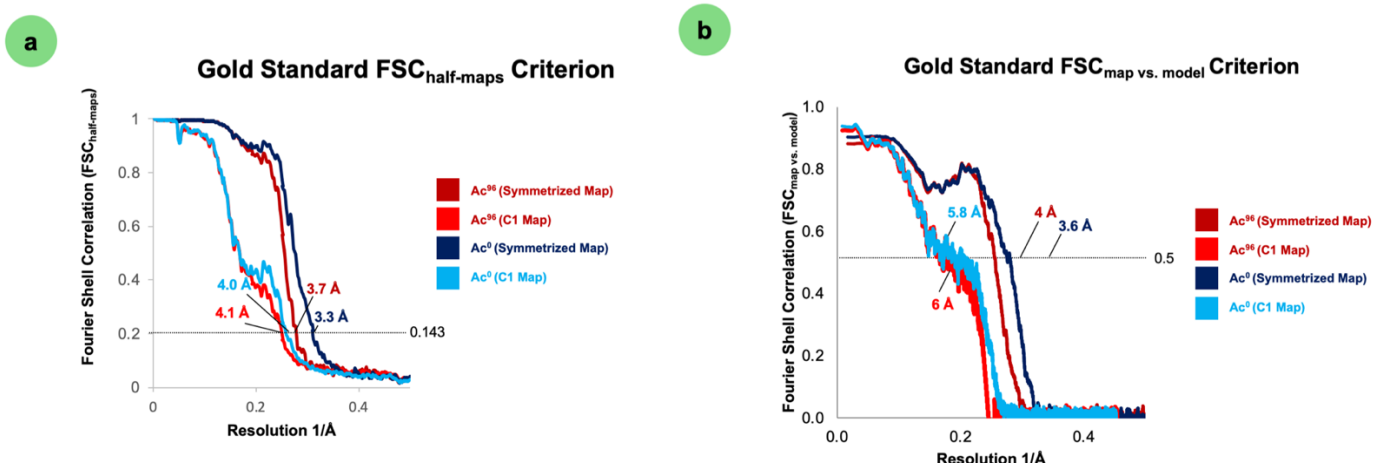

Supplemental Figure 5. Fourier Shell Correlation Plots.